arXiv:1601.00911v1 [astro-ph.HE] 5 Jan 2016

Fermi GBM Observations of V404 Cyg During its 2015 Outburst

P. A. Jenke[1], C. A. Wilson-Hodge[3], Jeroen Homan[4,5], P. Veres[1], M. S. Briggs[1], E. Burns[1], V. Connaughton[2], M. H. Finger[2], M. Hui[3]

ABSTRACT

V404 Cygni was discovered in 1989 by the *Ginga* X-ray satellite during its only previously observed X-ray outburst and soon after confirmed as a black hole binary. On June 15, 2015, the Gamma Ray Burst Monitor (GBM) triggered on a new outburst of V404 Cygni. We present 13 days of GBM observations of this latest outburst including Earth occultation flux measurements, spectral and temporal analysis. The Earth occultation fluxes reached 30 Crab with detected emission to 100 keV and determined, via hardness ratios, that the source was in a hard state. At high luminosity, spectral analysis between 8 and 300 keV showed that the electron temperature decreased with increasing luminosity. This is expected if the protons and electrons are in thermal equilibrium during an outburst with the electrons cooled by the Compton scattering of softer seed photons from the disk. However, the implied seed photon temperatures are unusually high, suggesting a contribution from another source, such as the jet. No evidence of state transitions is seen during this time period. Temporal analysis reveals the rich harmonic content of the outburst and confirmed that the source was in a hard state.

Subject headings: V404 Cyg,black holes,LMXB

[1]University of Alabama in Huntsville, Huntsville, AL 35805, USA

[2]Universities Space Research Association, Huntsville, AL 35805, USA.

[3]Marshall Space Flight Center, Huntsville, AL 35812, USA

[4]MIT Kavli Institute for Astrophysics and Space Research, 77 Massachusetts Avenue 37-582D, Cambridge, MA 02139, USA

[5]SRON, Netherlands Institute for Space Research, Sorbonnelaan 2, 3584 CA Utrecht, The Netherlands

1. Introduction

V404 Cygni, hereafter V404 Cyg, was first identified as an X-ray transient with the *Ginga* satellite during the 1989 flaring event (Makino et al. 1989). Using archival optical data, V404 Cyg was associated with what was thought to be a nova in two previous outbursts in 1938 and 1956. Optical observations after the 1989 flaring event revealed an orbital ephemeris with an orbital period of 6.5 days, an inclination of 67 degrees, and most importantly a mass function of 6.08 ± 0.16 (Casares and Charles 1994) making the source one of the first confirmed black hole systems with a black hole mass ~ 10 $M_{\odot}$. A radio parallax distance of 2.39 ± 0.14 kpc (Miller-Jones et al. 2009) allows precise monitoring of the intrinsic luminosity and makes this one of the closest known black hole systems. V404 Cyg's large separation from its companion along with optical Hα observations indicate that the system develops a very large accretion disk which contains an inordinate amount of material ensuring dramatic flares when the inner region of the accretion disk breaks down (Remillard and McClintock 2006).

At 18:31:38 UT on 2015, June 15, the *Swift* Burst Alert Telescope (BAT) triggered and located V404 Cyg (Barthelmy et al. 2015). Twenty eight minutes later, the *Fermi* Gamma Ray Burst Monitor (GBM) triggered on an X-ray source with a subsequent ground localization consistent with V404 Cyg.

2. Gamma Ray Burst Monitor

GBM is an all sky monitor whose primary objective is to extend the energy range over which gamma-ray bursts are observed in the Large Area Telescope (LAT) on *Fermi* (Meegan et al. 2009). GBM consists of 12 NaI detectors with a diameter of 12.7 cm and a thickness of 1.27 cm and two BGO detectors with a diameter and thickness of 12.7 cm. The NaI detectors have an energy range from 8 keV to 1 MeV while the BGOs extend the energy range to 40 MeV. GBM has three continuous data types: CTIME data with nominal 0.256-second time resolution and 8-channel spectral resolution used for event detection and localization, CSPEC data with nominal 4.096-second time resolution and 128-channel spectral resolution which is used for spectral modeling, and Continuous Time Tagged Event (CTTE) data which has a timing precision of 2μs. All three data types are utilized in the following analysis.

3. Observations

GBM triggered on V404 Cyg 169 times between June 15-27. The source reached a brightness of 30 Crab with emission to 300 keV. With an 8 sr field of view, GBM was able to observe the entire outburst with a duty cycle of 57%. GBM is not an imaging instrument but uses the differential response of its 12 NaI detectors to locate sources to a few degrees (Connaughton et al. 2015). Even though localization is possible, GBM's high background rates can make analysis challenging. To mitigate this limitation, three techniques are employed to analyze this source: the Earth occultation technique, choosing times of high signal to noise such as GBM triggered events, and using GBM's 2μs timing precision to extract temporal information from the data. These techniques and their results are detailed below.

3.1. Earth Occultation Observations

The Earth Occultation software, described in detail in Wilson-Hodge et al. (2012), fits the GBM CTIME data with a quadratic background plus models of occultation steps for the source of interest and any other bright sources occulting during the 4-minute fit window. The occultation step models incorporate atmospheric transmission and an assumed source flux model for each source in the fit. Independent fits are performed for each detector and each energy channel. For V404 Cyg, the assumed flux model was based on INTEGRAL SPI measurements (Rodriguez et al. 2015). Steps during solar flares, and when the constant background term was more than 3σ away from its Gaussian mean from pre-outburst data 2008 August to 2015 June 16 were removed from the analysis. High values of the constant term correlate with periods of high KP index (high particle activity). Figure 1 shows the light curve based on single occultation steps for V404 Cyg in the 8-300 keV band (GBM CTIME channels 0-4). V404 Cyg flux measurements in each energy channel were normalized to the average flux for the Crab nebula and pulsar for the time period 2015 June 17-July 2. Significant detections of a source within a single occultation step with GBM is unusual and is an indication of how bright V404 Cyg's flares were.

Remillard and McClintock (2006) described ways of defining black hole states, including a method based on radio properties, X-ray power density spectra, and hardness intensity diagrams. Hardness ratios were defined as 8.6-18.0 keV counts/5.0-8.6 keV counts measured with the *Rossi X-ray Timing Explorer (RXTE)* Proportional Counter Array, for which the Crab nebula yielded HR=0.68. Remillard and McClintock (2006) found that sources with HR>0.68, harder than the Crab Nebula, corresponded to the hard state in both McClintock and Remillard (2006) model and in the unified jet model (Fender et al. 2004) and HR<0.2

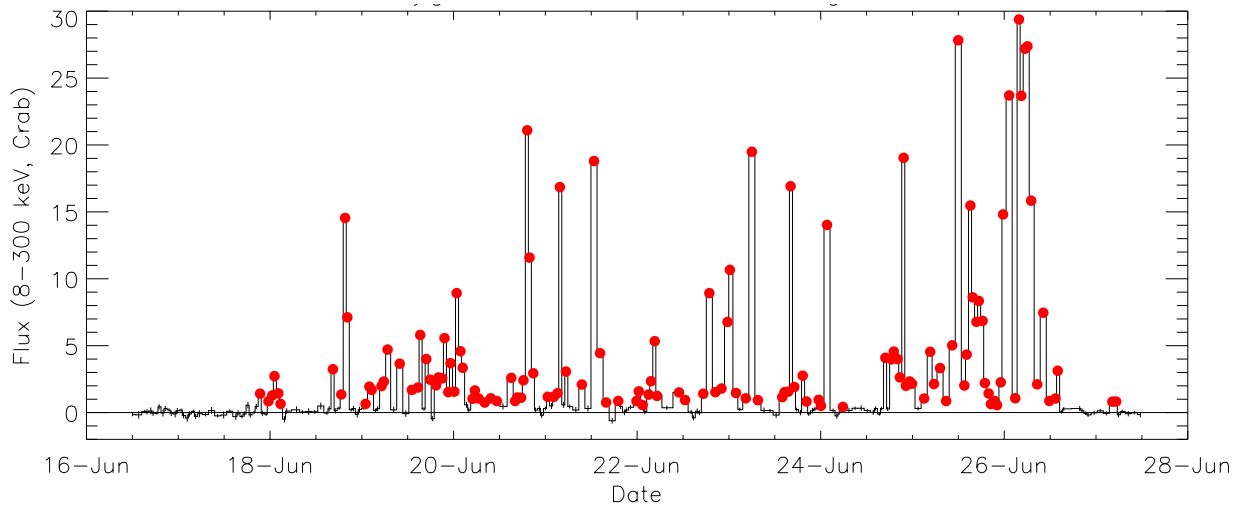

Fig. 1.— V404 Cyg light curve measured with Fermi GBM in the 8-300 keV band. Fluxes are normalized to GBM measurements of the Crab in the same band. Red circles indicate 3 σ or better detections in a single occupation step.

corresponded to the steep power law state. Further discussion in Remillard and McClintock (2006), and references therein, points out that in the hard state, an exponential cutoff near 100 keV is often found, while QPOs may or may not be present. Remillard and McClintock (2006) emphasize that luminosity is not a criterion for identifying X-ray states in either prescription.

To compare GBM measurements of V404 Cyg to these studies, hardness ratios were generated by dividing the single step flux measured in the 12-25 keV band by the flux in the 8-12 keV band, the lowest two bands available in GBM data and closest to the canonical *RXTE* bands, shown in Figure 2. The majority of the GBM hardness ratios (blue diamonds in Figure 2) are harder than the Crab, suggesting that V404 Cyg spent the majority of its outburst in the hard state even though it was emitting at a large fraction of its Eddington luminosity.

3.2. Spectral Analysis

We performed spectral analysis of the hard X-ray emission between 8 and 1000 keV in order to better understand the hot Comptonized corona surrounding the black hole.

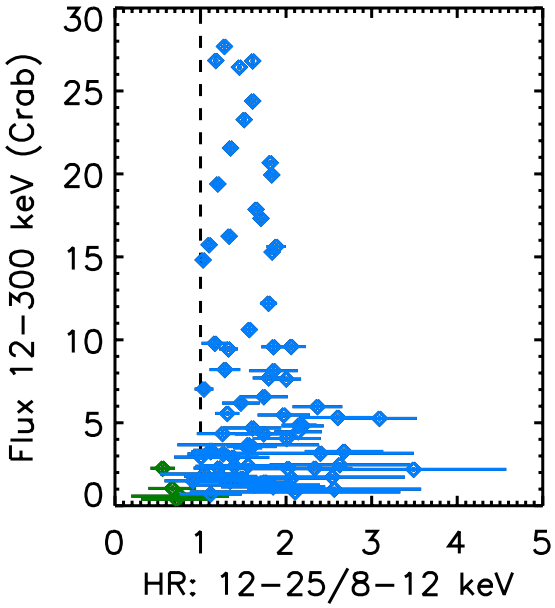

Fig. 2.— V404 Cyg hardness ratio (12-25 keV flux/8-12 keV flux) vs total flux in the 12-300 keV range. The dashed vertical line indicates the Crab hardness ratio for these bands. It is at 1.0 because the fluxes are normalized to the Crab. Blue diamonds indicate where V404 Cyg is harder than the Crab and green diamonds indicate where V404 Cyg is softer than the Crab.

3.2.1. Data Selection

GBM CSPEC data for the 169 V404 Cyg triggers were used for spectral analysis. Detectors with angles between the source and detector bore sight greater than 60 degrees were excluded. Using RMFIT, a forward-folding spectral analysis software often used in GBM gamma ray burst studies[1], a polynomial background was fit to each detector in each energy channel between 8 and 1000 keV using times before and after the flare. Times around the trigger times, when a flare was evident, were chosen and response matrices were created from a response model constructed from simulations incorporating the Fermi spacecraft mass model into GEANT4 (Agostinelli et al. 2003). Data selection was limited to 100 seconds before the trigger and 400 seconds after the trigger in order to ensure that an adequate background model could be fit and that the spacecraft response would not significantly change during the times of data selection. The background subtracted data was fit using RMFIT to the CompST model (Sunyaev and Titarchuk 1980) and the residuals in each detector were

[1]http://fermi.gsfc.nasa.gov/ssc/data/analysis/rmfit/

compared for consistency. Consistent residuals across detectors are an indication that the background selection is reasonable. Triggered events in which a good background model could not be constructed were rejected. For the remaining 155 events in which an acceptable spectral fit was possible, the background and the total spectrum were exported for analysis in XSPEC (Arnaud 1996).

3.2.2. Integrated Spectral Analysis Results

We chose spectral models to model the hot comptonized corona surrounding the black hole. The CompTT model (Titarchuk 1994) and the power law with high energy cut-off (POWER* HIGHECUT in XSPEC) were successful in representing the data although the cut-off energy could not always be well constrained. The results of the spectral fits to the CompTT and power law models are listed in Table 1. The burst number column (bn) is the date and fraction of the day at trigger time, YYMMDDFFF where YY is the two digit year, MM is the month, DD is the day, and FFF is the fraction of the day.

The CompTT model seed photon temperature, $kT_{\rm photon}$, is a free parameter and allows us to probe emission from the up-scattering of hot seed photons as apposed to the CompST model which assumes a cold distribution of seed photons. The CompTT model fits resulted in an average seed photon temperature of 5.9±1.3 keV. This is inconsistent with photons from an accretion disk ($kT_{\rm photon} < 1$ keV) and the cold photons assumed in the CompST model. The average optical depth, τ, is 1.45 ± 1.0 ($\bar{\sigma_\tau} = 0.56$) (see Figure 5) which is consistent with what is expected from the optically thick corona around a typical black hole binary (Malzac 2012). In the subsequent analysis, the optical depth is fixed to 1.45 in order to better constrain the electron and seed photon temperatures.

The POWER* HIGHECUT is useful for tracing the spectral variability between triggered flares. Figure 3 shows the evolution of the power law index throughout the outburst. In red are the weighted mean spectral indexes on half day time intervals. Although there is significant spectral evolution throughout the outburst period, there is no evidence for systematic softening or hardening of the spectrum during this period. The high energy cut-off, at times, was much lower (see Figure 4) than the 100 keV often observed for stellar mass black hole systems in the hard state (Malzac 2012; Remillard and McClintock 2006).

Initially a comptonized model by Sunyaev and Titarchuk (1980) (CompST in XSPEC) was chosen to model the emission from hot coronal electrons up-scattering the cold accretion disk photons. This model was chosen for its small number of parameters and its physical description of the emission region. The model was often a poor description of the GBM data,

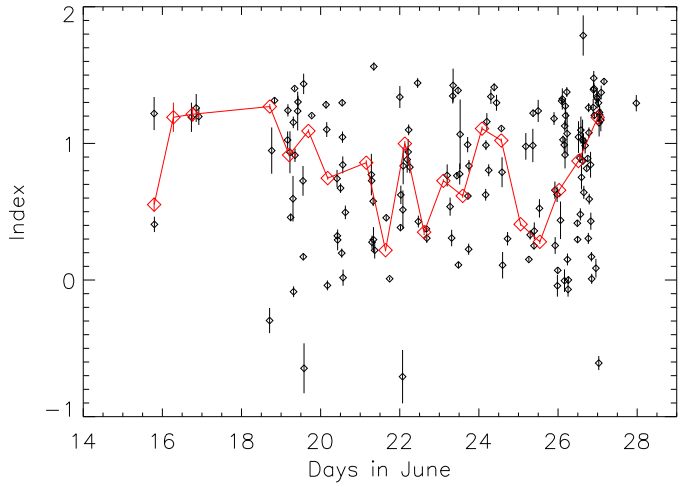

Fig. 3.— Evolution of the power law index for the high-E cutoff model throughout the outburst. The horizontal axis is the days in June while the vertical axis is the power law index from the power law with a high energy cut-off model fit to the data. In red are the weighted mean indexes on half day time intervals.

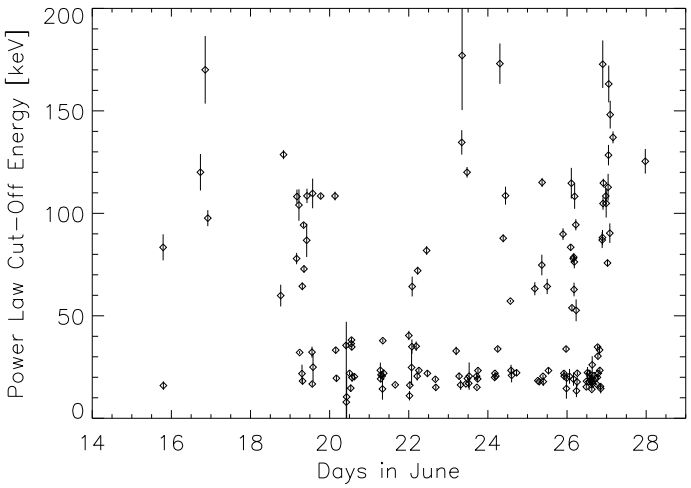

Fig. 4.— Evolution of the power law cut-off energy for the high-E cutoff model throughout the outburst. The horizontal axis is the days in June while the vertical axis is the power law index from the power law with a high energy cut-off model fit to the data.

especially during bright flares, and resulted in a large optical depth, tau (see Figure 5). Two absorption models, PHABS and PCFABS in XSPEC, were used to improve the model fit.

Both absorption models predicted extremely high absorption ($(100-1000)\times10^{22}$ cm^2) that is unsupported by soft X-ray observations (Motta et al. 2015). A reflection model (REFLECT in XSPEC) was also used to attempt to improve the CompST fit. The inclination of the the accretion disc was fixed to 67 degrees (Khargharia et al. 2010) and the redshift fixed to zero reflecting our proximity to the source. The new model was again preferred over just the CompST model but resulted in an unphysical reflection component that accounted for more than 400% of the emission. Other issues with the REFLECT*CompST model was, again, an excessively large optical depth that was often greater than 10. At this point the CompST model was abandoned in favor of the CompTT model.

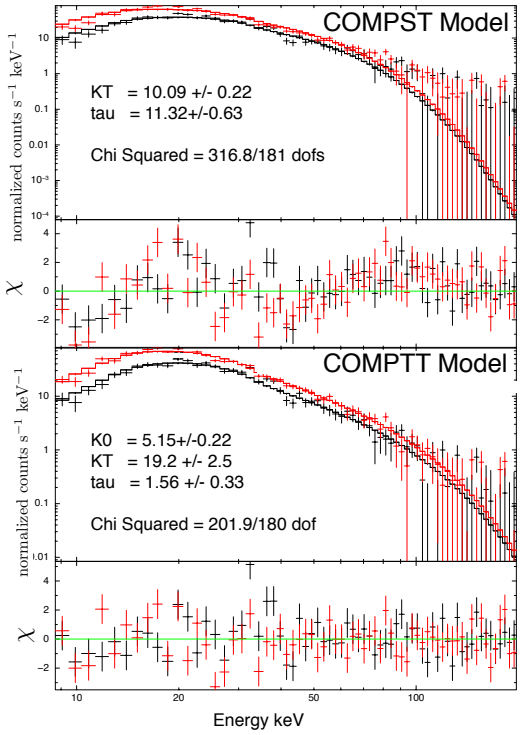

Fig. 5.— Time integrated spectral model fitting to the triggered event bn150626171. The figure on the top is the spectral fit using the CompST model with residuals below. The red and black points are the normalized counts from two of the NaI detectors while the red and black curves are the best fit model. The figure on the bottom is the spectral fit using the CompTT model with residuals below. The best fit parameters are given in the figures. The fit for the CompTT model is a significant improvement over the CompST model.

3.2.3. Time Resolved Spectral Analysis Results

Time resolved spectral analysis was performed on a few bright triggered flares to examine spectral variation within a flare. Ten second intervals were used for the time resolved analysis and an instrument response matrix was created for the center of each time interval. Only the CompTT model was used to fit the time resolved data. The trigger bn150625400 was chosen because it spanned a wide range of luminosities. The triggers bn150626685 and bn150626751 were chosen for their high luminosity while bn150626156 was chosen for its moderate luminosity. The optical depth was frozen at $\tau = 1.45$. Figure 6 shows how the electron and photon temperature evolve during the bright flare, bn150625400.

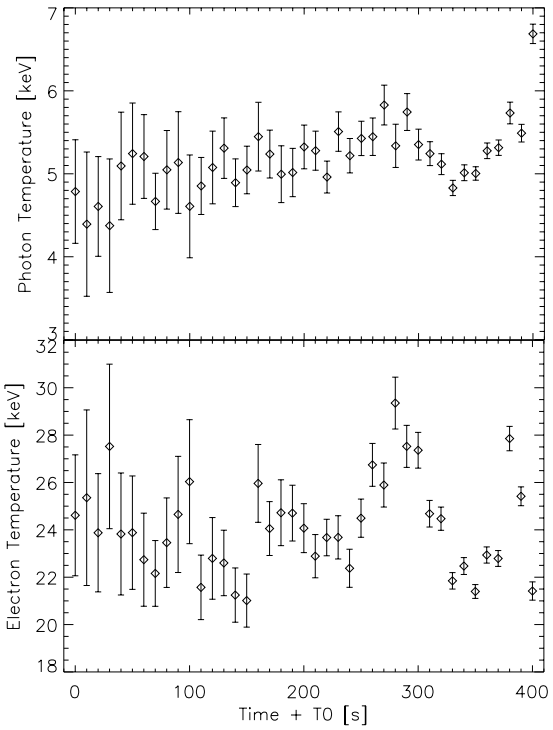

Fig. 6.— The top figure shows the evolution of the photon seed temperature during the GBM triggered flare, bn150625400, while the bottom figure shows the evolution of the electron temperature. The horizontal axis is time in seconds with T0 = 456917626.6 MET.

3.3. Temporal Data Analysis

3.3.1. Data Selection

GBM CTTE NaI data between 8 and 100 keV were selected between 2015 June 15–27. Times during SAA passage, times when V404 Cyg was occulted by the Earth and times during high particle activity were excluded from the analysis. The data selection resulted in good time intervals (GTIs) that were a few$\times$1000 seconds long. On a 100 second cadence, the selected CTTE data were combined for all the detectors which had a source to detector bore sight angle of less than 60 degrees, and binned to 1 ms, to produce 100 second long light curves. The light curves were Fourier transformed producing power spectra with a frequency range of 0.01–500 Hz. The power spectra for each GTI were averaged to reduce the variance resulting in 214 power spectra.

Although source and background count rates were not available for all observations, the power spectra that were studied in detail (see below), were all rms normalized (Belloni and Hasinger 1990; Miyamoto et al. 1991). We note, however, that the source and background rates used for the rms normalization are estimates based on the spectral analysis.

3.3.2. Temporal Analysis Results

All 214 power spectra were visually inspected. For the ones from low-count-rate observations no significant power is seen. However, the power spectra from observations during bright flares are of high quality and show significant power. In Figure 7 we show five normalized power spectra from the period of June 26–27, during which the source reached its peak brightness. They are representative of the power spectra during other flares. The power spectra are dominated by strong broad features, similar to *Ginga* power spectra of V404 Cyg during its 1989 outburst (Oosterbroek et al. 1997). No narrow QPO features were seen. The integrated fractional rms in the 0.01–100 Hz band ranged from $\sim$35% to $\sim$50%.

Like the *Ginga* power spectra, we find that the GBM power spectra of V404 Cyg can be fitted well with two or three broad Lorentzians, where we define the Lorentzians as $(P(\nu) = (r^2\Delta/\pi)[\Delta^2 + (\nu - \nu_0)^2]^{-1})$. Here ν_0 is the centroid frequency, Δ the half-width-at-half-maximum, and r the integrated fractional rms (from $-\infty$ to ∞). Instead of ν_0 and Δ we will quote the frequency ν_{max} at which the Lorentzian attains its maximum in $\nu P(\nu)$ and the quality factor, Q, where $\nu_{max} = \nu_0(1 + 1/4Q^2)^{1/2}$ and $Q = \nu_0/2\Delta$.

The Lorentzian fits to the power spectra are shown in Figure 7. As can be seen, the Lorentzians are well-separated in frequency. Small shifts in the frequencies of the Lorentzians

are seen, but the overall shape of the power spectra remained the same, with perhaps an exception in the bottom panel of Figure 7. This was also mostly the case for the *Ginga* power spectra reported by Oosterbroek et al. (1997), who only observed one clear exception from the usual shape in their set of power spectra. The ν_{max} ranges for the three Lorentzians are: ∼0.015–0.04 Hz, ∼0.17–0.82 Hz, and ∼1.7–4.8 Hz. The Q-values of the broad noise features were less than 0.75 and in most cases were fixed at 0. The fractional rms amplitudes of the low-, mid-, and high-frequency Lorentzians were ∼30–35%, ∼15–30%, and ∼15–23%, respectively. The quality of the June 27 power spectrum in Figure 7 was not high enough to separately fit the two highest-frequency components, and only two Lorentzians were used to fit this power spectrum.

4. Discussion

For a $10M_{\odot}$ black hole the Schwarzschild radius is $R_S = 3 \times 10^6$ cm and the Eddington luminosity is $L_{\rm EDD} = 1.26 \times 10^{39}$ erg s^{-1}. The luminosities calculated for GBM data are from 10-1000 keV. Significant flux is expected below 10 keV therefore our luminosities represent lower limits to the bolometric luminosity. It is probable that V404 Cyg reached or exceeded the Eddington luminosity during the 2015 outburst.

4.1. Physical Model for the Hard X-ray Emission

We find a clear anti-correlation between the GBM flux and the electron temperature of the CompTT model. We present this behavior in the equivalent $L/L_{\rm EDD} - kT_e$ diagram (see Figure 8). This correlation is present both in the brighter flares and when considering the entire duration of the current V404 Cyg flaring activity.

Overall, the electron temperature values show large variations and no obvious correlation up to $L \lesssim 0.15 L_{\rm EDD}$. For $L > 0.15 L_{\rm EDD}$ a clear anti-correlation emerges, and the scatter in T_e decreases visibly (see Figure 8). Individual outbursts' show a similar behavior, when well sampled (trigger bn150625400 in Figure 9).

The correlation between the electron temperature and luminosity has already been noted in the case of GX 339-4 by Miyakawa et al. (2008). Using GBM observations of V404 Cyg, we can populate a larger swath of the $L - kT_e$ diagram and find their interpretation valid here as well with minor modifications. We envision a population of protons in thermal equilibrium with hot electrons which are in turn responsible for the inverse Compton up-scattering of the soft thermal photons from the disk or base of the jet, resulting in the gamma-ray photons.

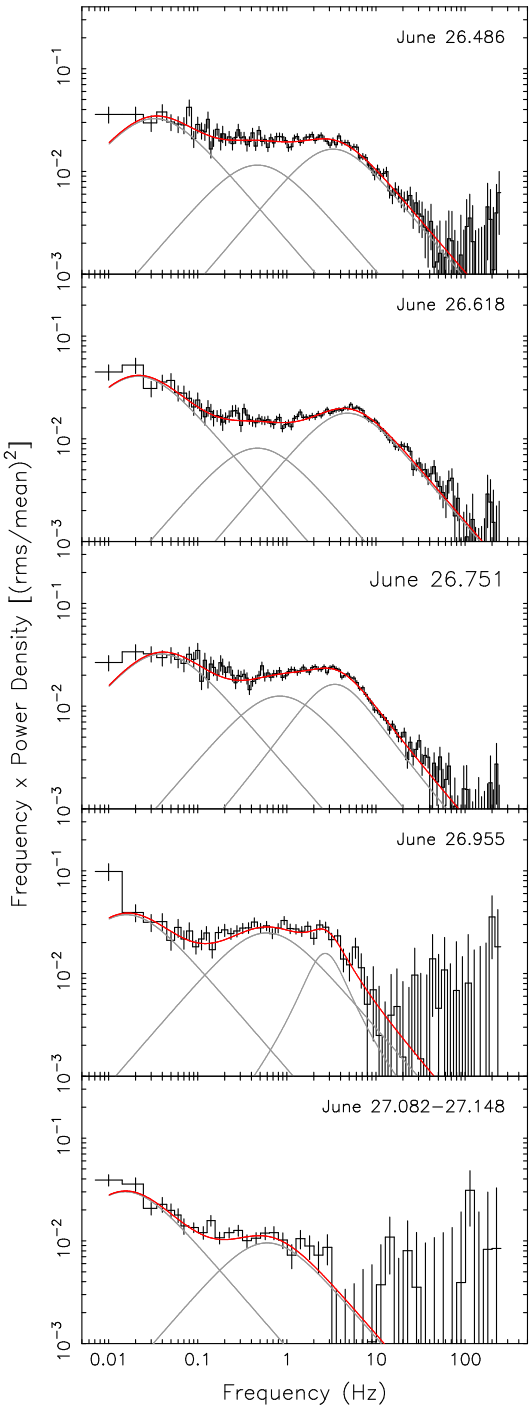

Fig. 7.— A sequence of power spectra of V404 Cyg from June 26–27. Models fits with two or three Lorentzian are shown in red; individual Lorentzians are plotted in gray. Corresponding dates are shown in the upper right corners.

In order to determine which processes drive the bursting activity, we calculate relevant timescales. The electron-proton relaxation timescale can be calculated as (Spitzer 1962):

$$t_{pe} = \frac{3m_p(kT_p/m_p + kT_e/m_e)^{3/2}}{4\pi^{1/2}m_e^{1/2}q_e^4 n_e \ln\Lambda} = 5.3\times10^{-3}\left(\frac{R}{10\ R_S}\right)\left(\frac{kT_e}{30\ \mathrm{keV}}\right)^{3/2}\left(\frac{\tau}{1.45}\right)^{-1}\mathrm{s} \quad (1)$$

where n_e is the particle number density, $\ln\Lambda = 16.1 + \ln[(kT_e/\ 30\mathrm{keV})(n_e/10^{17}\mathrm{cm}^{-3})^{-1/2}]$ is the Coulomb logarithm, T_e and T_p are the electron and proton temperatures respectively. Electrons and protons establish a Maxwellian distribution on this timescale. For the numerical value, we have assumed $T_e > \frac{m_e}{m_p}T_p$ and $\tau \approx Rn_e\sigma_T$. Henceforth, we use $10R_S$ for the size of the emission region.

Electrons will lose energy to soft photons through inverse Compton scattering on a timescale

$$t_{\mathrm{IC}} = \frac{3m_ec^2}{8\sigma_T L\tau/(\pi R^2)} = 3.6\times10^{-6}\left(\frac{L/L_{\mathrm{EDD}}}{0.2}\right)^{-1}\left(\frac{R}{10\ R_S}\right)^{2}\left(\frac{\tau}{1.45}\right)^{-1}\mathrm{s} \quad (2)$$

The advection timescale, or the time in which electrons are swallowed by the black hole (Mahadevan and Quataert 1997) can be calculated e.g. in the advection dominated accretion flow model (Narayan and Yi 1994):

$$t_{\mathrm{adv}} \approx \frac{R^2}{\alpha H^2\sqrt{GM/R^3}} \quad (3)$$

$$= 0.4\left(\frac{R/H}{0.2}\right)^{2}\left(\frac{R}{10\ R_S}\right)^{3/2}\left(\frac{\alpha}{0.3}\right)^{-1}\mathrm{s}, \quad (4)$$

where H is the height of the disk, assumed to be a fraction 0.2 of the radius, and α is the viscosity parameter scaled to 0.3.

Out of these three timescales, the Compton cooling is the shortest. Based on the above equations the proton-electron equilibrium timescale is shorter than the advection timescale indicating the former is the more efficient process. However the value of H, α and the emission region size assumed here, $10R_S$ have large uncertainties allowing t_{adv} to be of the same order as t_{pe} (e.g. for $H/R \approx \alpha \approx 1$, and $R \approx 3R_S$). If this is the case, about an equal fraction of electrons will be available for IC up scattering and for advection. As the luminosity increases, IC cooling becomes more effective, decreasing the temperature of the electrons. Colder electrons result in more effective proton-electron collisional relaxation,

while the advection efficiency does not vary with electron temperature. Thus eventually the two main processes will be the electron proton interaction and the IC cooling of the electrons.

If we assume a steady state, the energy transferred per unit volume and unit time from protons to electrons will equal the energy lost by electrons through Compton cooling, following Inoue (1994); Miyakawa et al. (2008), yields:

$$\frac{3/2nkT_p}{t_{\rm pe}} = \frac{4kT_eLn_e\sigma_T}{\pi R^2 m_e c^2}. \tag{5}$$

We will assume a constant proton temperature and fix the optical depth at $\tau = 1.45$. We also assume as before: $T_e/m_e > T_p/m_p$ which, for electron temperatures of $\sim$ 30 keV gives $T_p \lesssim 60$ MeV. The approximate proton temperature can be estimated from the release of gravitational potential energy ($GM/R = kT_p/m_p$). We get consistently $T_p \approx 46(R/10\ R_S)^{-1}(M/10M_\odot)$MeV

From Equation 5, using the expression for $t_{\rm pe}$, we find $T_e \propto L^{-2/5}$, which is in remarkable agreement with both the time resolved spectra (Figure 9) and considering all the bursts (see Figure 8).

This observed relation between the electron temperature and luminosity suggests that during an outburst the electrons and protons are in thermal equilibrium and the electrons are cooled by the Compton scattering of thermal photons from the disk. V404 Cyg is yet another example among accreting black hole systems (both black hole binaries and AGN) where the collisional heating of electrons by protons is a dominant process.

Similarly to Roques et al. (2015a), the seed photon temperature obtained from the CompTT model is unusually high. The highest temperature from a thermally radiating disk is $kT_{\rm photon} \lesssim 1$ keV, while we have an approximately constant $kT_{\rm photon} = 5.9 \pm 1.3$ keV. This suggests the seed photons might not originate solely from the disk, but from another source as well (e.g. synchroton photons from the jet (Markoff et al. 2005)). A high seed photon temperature (7 keV) was also measured using INTEGRAL data (Roques et al. 2015b).

We note that for the time resolved spectra the onset of the correlation appears to start at higher luminosities ($0.35 - 0.5L_{\rm EDD}$, (see Figures 9, 10, 11) while the time integrated correlation is valid for $L > 0.15L_{\rm EDD}$. This can be explained by the longer integration times for the data points ($\sim$500s as apposed to 10s), resulting in more accurate spectral parameters for $L/L_{\rm EDD}$ in the range of 0.15-0.35. For the time resolved cases the error on the parameters increases for this range of luminosities, suppressing the correlation.

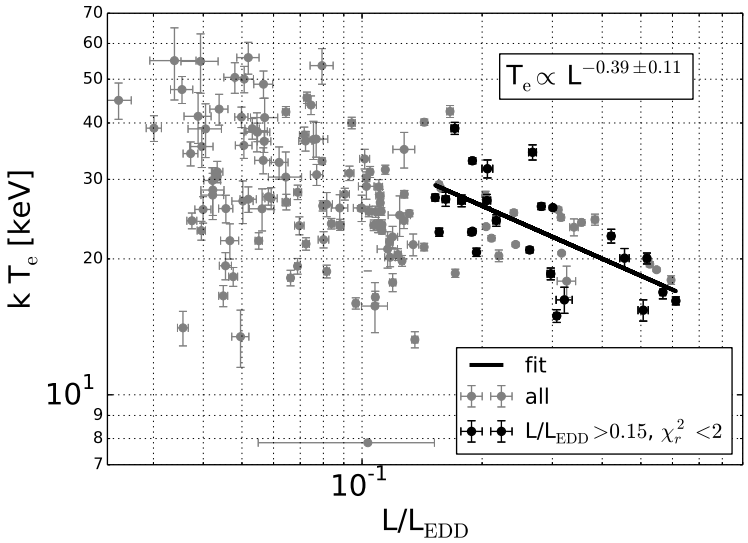

Fig. 8.— Luminosity and electron temperature for all the triggered intervals. Gray points mark all the intervals, black points indicate bright ($L > 0.15 L_{\rm EDD}$) and reliable fits ($\chi^2_\mu < 2$).

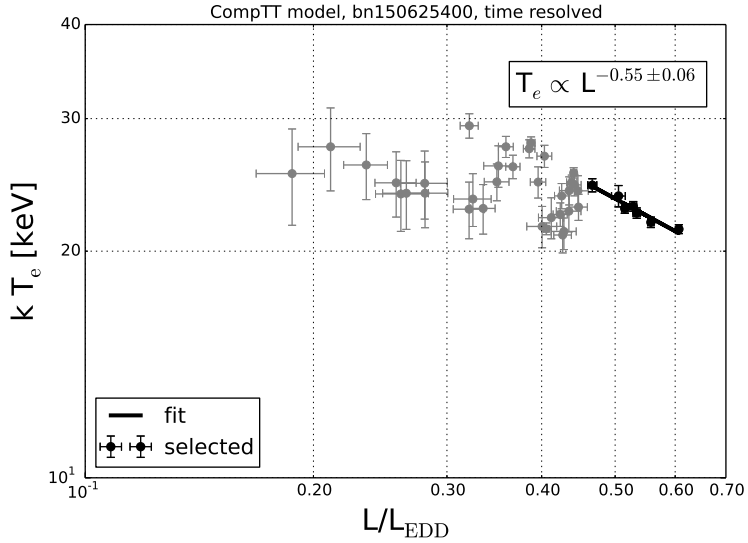

Fig. 9.— Luminosity and electron temperature for an individual trigger. Gray points mark all the intervals, black points indicate bright ($L > 0.5 L_{\rm EDD}$) and reliable fits ($\chi^2{}_\mu < 2$).

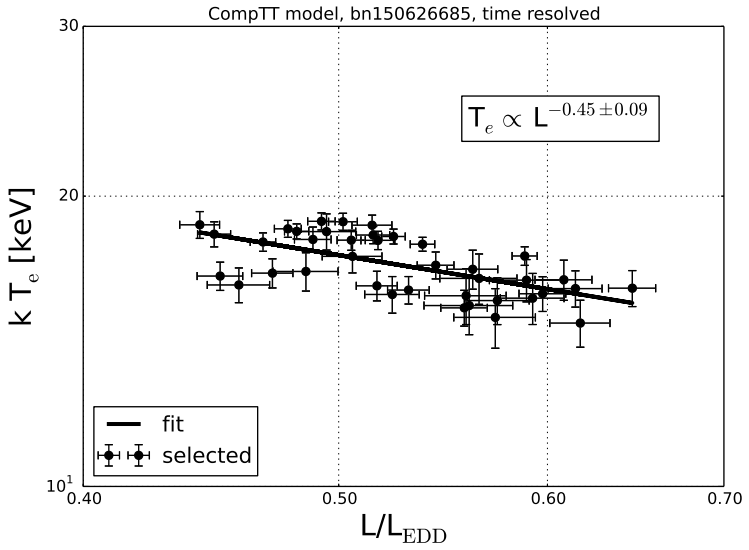

Fig. 10.— A further example of a time resolved fit. The anti-correlation exists for the entire flare because it remained above $0.45L_{Edd}$.

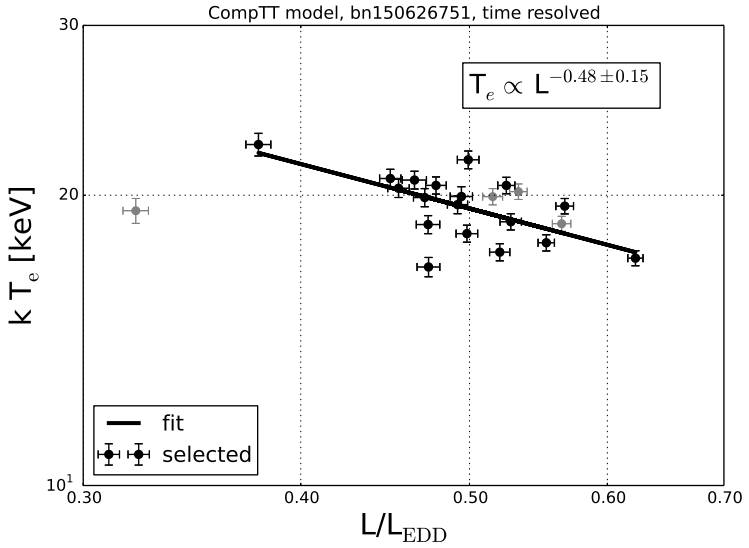

Fig. 11.— Luminosity and electron temperature for individual triggers. Gray points mark all the intervals, black points indicate bright ($L > 0.5L_{\rm EDD}$) and reliable fits ($\chi^2_\mu < 2$).

4.2. Temporal Analysis

The GBM power spectra of V404 Cyg show a strong similarity to those obtained with *Ginga* during the source's 1989 outburst. They are also similar in shape and strength to those of black hole X-ry binaries, such as Cyg X-1 and GX 339–4, in their hard states (Nowak 2000). The power spectra of these sources are dominated by broad Lorentzians as well, in the frequency range that we analyzed for V404 Cyg (0.01–500 Hz). In Figure 12 we show a comparison between an averaged power spectrum from GX 339–4 in its hard state (from *RXTE* data) and one from V404 Cyg (June 26.71, see middle panel in Figure 7). The shapes of these power spectra are very similar, especially at the high-frequency end. We suspect that relatively stronger variability at the low-frequency end in V404 Cyg may be the result of the strong flaring activity of V404 Cyg seen on the corresponding time scales. Overall, the shape and strength of the power spectra supports the occultation hardness ratio analysis conclusion that V404 Cyg was observed in the hard state.

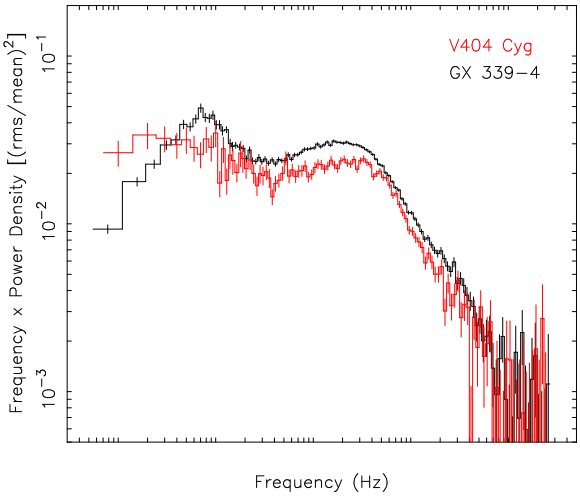

Fig. 12.— A comparison of an averaged *RXTE* power spectrum from the hard state of GX 339–4 (black) with a GBM power spectrum of V404 Cyg from June 26.751 (red).

5. Conclusion

There is no evidence in the spectral analysis for an onset of a state change during the observed time interval. Spectral analysis indicates that the collisional heating of electrons by protons is the dominant process resulting in the observed Comptonized spectrum. The seed photon temperature exceeds what is expected from an accretion disk and may be due

to synchrotron photons from the base of the jet or perhaps there is some other method of energizing the photons of the inner disk. In all, this outburst is very similar to the one that occurred in 1989 but remains remarkable among black hole outburst for its intrinsic high luminosity and high photon seed temperature.

REFERENCES

Agostinelli, S., Allison, J., Amako, K., Apostolakis, J., Araujo, H., Arce, P., Asai, M., Axen, D., Banerjee, S., Barrand, G., Behner, F., Bellagamba, L., Boudreau, J., Broglia, L., Brunengo, A., Burkhardt, H., Chauvie, S., Chuma, J., Chytracek, R., Cooperman, G., Cosmo, G., Degtyarenko, P., Dell'Acqua, A., Depaola, G., Dietrich, D., Enami, R., Feliciello, A., Ferguson, C., Fesefeldt, H., Folger, G., Foppiano, F., Forti, A., Garelli, S., Giani, S., Giannitrapani, R., Gibin, D., Cadenas, J. G., Gonzlez, I., Abril, G. G., Greeniaus, G., Greiner, W., Grichine, V., Grossheim, A., Guatelli, S., Gumplinger, P., Hamatsu, R., Hashimoto, K., Hasui, H., Heikkinen, A., Howard, A., Ivanchenko, V., Johnson, A., Jones, F., Kallenbach, J., Kanaya, N., Kawabata, M., Kawabata, Y., Kawaguti, M., Kelner, S., Kent, P., Kimura, A., Kodama, T., Kokoulin, R., Kossov, M., Kurashige, H., Lamanna, E., Lampn, T., Lara, V., Lefebure, V., Lei, F., Liendl, M., Lockman, W., Longo, F., Magni, S., Maire, M., Medernach, E., Minamimoto, K., de Freitas, P. M., Morita, Y., Murakami, K., Nagamatu, M., Nartallo, R., Nieminen, P., Nishimura, T., Ohtsubo, K., Okamura, M., O'Neale, S., Oohata, Y., Paech, K., Perl, J., Pfeiffer, A., Pia, M., Ranjard, F., Rybin, A., Sadilov, S., Salvo, E. D., Santin, G., Sasaki, T., Savvas, N., Sawada, Y., Scherer, S., Sei, S., Sirotenko, V., Smith, D., Starkov, N., Stoecker, H., Sulkimo, J., Takahata, M., Tanaka, S., Tcherniaev, E., Tehrani, E. S., Tropeano, M., Truscott, P., Uno, H., Urban, L., Urban, P., Verderi, M., Walkden, A., Wander, W., Weber, H., Wellisch, J., Wenaus, T., Williams, D., Wright, D., Yamada, T., Yoshida, H., and Zschiesche, D.: 2003, *Nuclear Instruments and Methods in Physics Research Section A: Accelerators, Spectrometers, Detectors and Associated Equipment* **506(3)**, 250

Arnaud, K. A.: 1996, in G. H. Jacoby and J. Barnes (eds.), *Astronomical Data Analysis Software and Systems V*, Vol. 101 of *Astronomical Society of the Pacific Conference Series*, p. 17

Barthelmy, S. D., Chester, M. M., Malesani, D., and Page, K. L.: 2015, *GRB Coordinates Network* **17949**, 1

Belloni, T. and Hasinger, G.: 1990, *A&A* **227**, L33

Casares, J. and Charles, P. A.: 1994, in S. Holt and C. S. Day (eds.), *The Evolution of X-ray Binariese*, Vol. 308 of *American Institute of Physics Conference Series*, p. 107

Connaughton, V., Briggs, M. S., Goldstein, A., Meegan, C. A., Paciesas, W. S., Preece, R. D., Wilson-Hodge, C. A., Gibby, M. H., Greiner, J., Gruber, D., Jenke, P., Kippen, R. M., Pelassa, V., Xiong, S., Yu, H.-F., Bhat, P. N., Burgess, J. M., Byrne, D., Fitzpatrick, G., Foley, S., Giles, M. M., Guiriec, S., van der Horst, A. J., von Kienlin, A., McBreen, S., McGlynn, S., Tierney, D., and Zhang, B.-B.: 2015, *ApJS* **216**, 32

Fender, R. P., Belloni, T. M., and Gallo, E.: 2004, *MNRAS* **355**, 1105

Inoue, H.: 1994, in T. Courvoisier and A. Blecha (eds.), *Multi-Wavelength Continuum Emission of AGN*, Vol. 159 of *IAU Symposium*, pp 73–82

Khargharia, J., Froning, C. S., and Robinson, E. L.: 2010, *ApJ* **716**, 1105

Mahadevan, R. and Quataert, E.: 1997, *ApJ* **490**, 605

Makino, F., Wagner, R. M., Starrfield, S., Buie, M. W., Bond, H. E., Johnson, J., Harrison, T., and Gehrz, R. D.: 1989, *IAU Circ.* **4786**, 1

Malzac, J.: 2012, *International Journal of Modern Physics Conference Series* **8**, 73

Markoff, S., Nowak, M. A., and Wilms, J.: 2005, *ApJ* **635**, 1203

McClintock, J. E. and Remillard, R. A.: 2006, *Black hole binaries*, pp 157–213

Meegan, C., Lichti, G., Bhat, P. N., Bissaldi, E., Briggs, M. S., Connaughton, V., Diehl, R., Fishman, G., Greiner, J., Hoover, A. S., van der Horst, A. J., von Kienlin, A., Kippen, R. M., Kouveliotou, C., McBreen, S., Paciesas, W. S., Preece, R., Steinle, H., Wallace, M. S., Wilson, R. B., and Wilson-Hodge, C.: 2009, *ApJ* **702**, 791

Miller-Jones, J. C. A., Jonker, P. G., Dhawan, V., Brisken, W., Rupen, M. P., Nelemans, G., and Gallo, E.: 2009, *ApJ* **706**, L230

Miyakawa, T., Yamaoka, K., Homan, J., Saito, K., Dotani, T., Yoshida, A., and Inoue, H.: 2008, *PASJ* **60**, 637

Miyamoto, S., Kimura, K., Kitamoto, S., Dotani, T., and Ebisawa, K.: 1991, *ApJ* **383**, 784

Motta, S., Beardmore, A., Oates, S., Sanna, N. P. M. K. A., Kuulkers, E., Kajava, J., and Sanchez-Fernanedz, C.: 2015, *The Astronomer's Telegram* **7665**, 1

Narayan, R. and Yi, I.: 1994, *ApJ* **428**, L13

Nowak, M. A.: 2000, *MNRAS* **318**, 361

Oosterbroek, T., van der Klis, M., van Paradijs, J., Vaughan, B., Rutledge, R., Lewin, W. H. G., Tanaka, Y., Nagase, F., Dotani, T., Mitsuda, K., and Miyamoto, S.: 1997, *A&A* **321**, 776

Remillard, R. A. and McClintock, J. E.: 2006, *ARA&A* **44**, 49

Rodriguez, J., Cadolle Bel, M., Alfonso-Garzón, J., Siegert, T., Zhang, X.-L., Grinberg, V., Savchenko, V., Tomsick, J. A., Chenevez, J., Clavel, M., Corbel, S., Diehl, R., Domingo, A., Gouiffès, C., Greiner, J., Krause, M. G. H., Laurent, P., Loh, A., Markoff, S., Mas-Hesse, J. M., Miller-Jones, J. C. A., Russell, D. M., and Wilms, J.: 2015, *A&A* **581**, L9

Roques, J.-P., Jourdain, E., Bazzano, A., Fiocchi, M., Natalucci, L., and Ubertini, P.: 2015a, *ApJ* **813**, L22

Roques, J.-P., Jourdain, E., Bazzano, A., Fiocchi, M., Natalucci, L., and Ubertini, P.: 2015b, *ApJ* **813**, L22

Spitzer, L.: 1962, *Physics of Fully Ionized Gases*

Sunyaev, R. A. and Titarchuk, L. G.: 1980, *A&A* **86**, 121

Titarchuk, L.: 1994, *ApJ* **434**, 570

Wilson-Hodge, C. A., Case, G. L., Cherry, M. L., Rodi, J., Camero-Arranz, A., Jenke, P., Chaplin, V., Beklen, E., Finger, M., Bhat, N., Briggs, M. S., Connaughton, V., Greiner, J., Kippen, R. M., Meegan, C. A., Paciesas, W. S., Preece, R., and von Kienlin, A.: 2012, *ApJS* **201**, 33

This preprint was prepared with the AAS LaTeX macros v5.2.

Table 1:: V404 Cyg Spectral Modeling Results

bn	Index[a]	E_{cut}[a] keV	Luminosity[a,b] 10^{37}erg cm^{-2}	Chi/dof	Electron Temp.[c] keV	Seed Photon Temp.[c] keV	Luminosity[b,c] 10^{37}erg cm^{-2}	χ^2/dof
150615791	1.21 ± 0.12	83.4 ± 6.3	4.16 ± 0.43	229/181	6.67 ± 0.88	35.4 ± 3.5	5.07 ± 0.38	207/181
150615798	0.407 ± 0.056	15.9 ± 2.0	4.57 ± 0.10	465/365	4.68 ± 0.24	24.29 ± 0.97	4.79 ± 0.11	454/365
150616734	1.19 ± 0.10	120.0 ± 8.9	4.39 ± 0.48	387/365	7.2 ± 1.0	41.3 ± 5.3	4.96 ± 0.35	391/365
150616855	1.25 ± 0.10	$170.0 \pm 16.$	4.28 ± 0.58	281/273	6.5 ± 1.2	54.7 ± 8.2	5.03 ± 0.55	280/273
f 150616921	1.196 ± 0.061	97.6 ± 3.9	3.16 ± 0.12	202/181	6.70 ± 0.52	38.9 ± 2.5	3.84 ± 0.17	176/181
150618710	-0.296 ± 0.092	$0.00 \pm 279.$	$3.3 \pm 23.$	458/365	2.83 ± 0.78	47.4 ± 3.2	4.52 ± 0.32	402/365
150618763	0.94 ± 0.16	59.8 ± 5.3	6.4 ± 1.5	506/181	7.77 ± 0.87	25.8 ± 2.7	7.18 ± 0.54	495/181
150618834	1.314 ± 0.022	128.6 ± 2.2	7.04 ± 0.11	459/181	6.67 ± 0.22	42.3 ± 1.1	8.24 ± 0.14	217/181
150619165	1.024 ± 0.062	77.9 ± 2.7	4.79 ± 0.18	191/181	8.12 ± 0.45	31.1 ± 1.7	5.54 ± 0.19	160/181
150619173	1.241 ± 0.044	108.1 ± 3.4	5.29 ± 0.21	248/181	6.40 ± 0.41	41.2 ± 2.1	6.37 ± 0.24	224/181
150619224	0.93 ± 0.15	104.0 ± 7.6	4.32 ± 0.69	326/273	9.9 ± 1.5	38.8 ± 5.2	5.18 ± 0.53	318/273
150619242	0.458 ± 0.028	32.11 ± 0.69	18.15 ± 0.14	1568/365	5.400 ± 0.086	29.21 ± 0.36	19.94 ± 0.18	1014/365
150619301	0.59 ± 0.16	21.8 ± 4.3	5.73 ± 0.65	215/181	5.15 ± 0.51	21.9 ± 1.9	5.96 ± 0.35	213/181
150619309	1.153 ± 0.042	64.4 ± 1.9	18.44 ± 0.42	372/181	6.59 ± 0.25	27.11 ± 0.97	20.72 ± 0.49	246/181
150619316	-0.085 ± 0.039	18.1 ± 1.5	24.72 ± 0.43	150/ 89	6.67 ± 0.20	26.93 ± 0.84	26.29 ± 0.46	130/ 89
150619342	1.402 ± 0.014	94.2 ± 1.0	21.46 ± 0.19	681/181	6.16 ± 0.12	32.98 ± 0.49	24.18 ± 0.23	265/181
150619352	0.913 ± 0.049	72.8 ± 1.7	7.52 ± 0.19	578/181	9.56 ± 0.35	26.7 ± 1.0	8.26 ± 0.19	531/181
150619420	1.23 ± 0.14	86.8 ± 8.1	7.47 ± 0.90	188/181	7.8 ± 1.1	30.3 ± 4.1	8.23 ± 0.80	189/181
150619427	1.303 ± 0.045	108.5 ± 3.5	8.18 ± 0.29	225/181	6.38 ± 0.41	36.4 ± 1.8	9.23 ± 0.27	208/181
150619554	0.72 ± 0.10	32.2 ± 2.6	17.0 ± 1.0	418/181	6.08 ± 0.35	21.5 ± 1.1	17.17 ± 0.55	414/181
150619561	0.170 ± 0.023	16.74 ± 0.96	34.28 ± 0.37	389/181	5.31 ± 0.11	26.14 ± 0.42	36.00 ± 0.34	276/181
150619570	1.435 ± 0.074	109.7 ± 7.2	8.55 ± 0.53	181/181	5.37 ± 0.65	36.8 ± 3.2	9.81 ± 0.72	168/181
150619580	-0.64 ± 0.18	24.9 ± 6.8	5.16 ± 0.64	119/ 89	10.3 ± 1.0	27.6 ± 3.2	5.40 ± 0.31	119/ 89
150619774	1.203 ± 0.013	108.4 ± 1.0	15.47 ± 0.14	1842/457	7.29 ± 0.12	40.16 ± 0.63	18.31 ± 0.19	1560/457
150620136	1.283 ± 0.027	108.4 ± 2.1	16.21 ± 0.31	372/181	8.84 ± 0.23	27.82 ± 0.53	16.32 ± 0.31	309/181
150620154	1.101 ± 0.054	33.2 ± 1.4	13.21 ± 0.30	418/271	5.11 ± 0.17	19.46 ± 0.63	12.88 ± 0.28	473/271
150620171	-0.039 ± 0.035	19.5 ± 1.3	12.67 ± 0.16	584/365	6.91 ± 0.18	25.47 ± 0.67	13.30 ± 0.23	559/365
150620414	0.742 ± 0.063	35.5 ± 1.5	21.29 ± 0.48	192/ 89	5.13 ± 0.19	26.89 ± 0.79	22.72 ± 0.42	136/ 89
150620421	0.323 ± 0.026	$7.8 \pm 39.$	$13.5 \pm 13.$	241/181	4.78 ± 0.15	23.74 ± 0.64	13.68 ± 0.26	312/181
150620429	0.293 ± 0.075	$10.4 \pm 10.$	4.92 ± 0.51	528/457	4.50 ± 0.41	25.7 ± 1.7	5.10 ± 0.21	529/457
150620503	0.672 ± 0.035	21.95 ± 0.91	21.86 ± 0.21	495/181	5.58 ± 0.11	18.58 ± 0.38	21.90 ± 0.23	392/181
150620533	0.196 ± 0.033	14.6 ± 1.8	26.86 ± 0.47	346/181	5.67 ± 0.19	24.32 ± 0.71	27.76 ± 0.39	344/181
150620545	1.297 ± 0.020	36.39 ± 0.59	25.01 ± 0.18	795/ 89	3.666 ± 0.055	23.57 ± 0.23	26.17 ± 0.19	238/ 89
150620552	1.045 ± 0.041	38.1 ± 1.0	18.08 ± 0.23	615/273	4.03 ± 0.11	27.34 ± 0.47	19.51 ± 0.28	436/273
150620559	0.842 ± 0.062	34.8 ± 1.5	13.71 ± 0.33	706/457	5.35 ± 0.19	23.63 ± 0.76	14.03 ± 0.28	720/457
150620567	0.017 ± 0.059	19.8 ± 2.1	4.94 ± 0.11	561/457	7.26 ± 0.31	23.1 ± 1.1	5.05 ± 0.13	563/457
150620625	0.495 ± 0.049	20.3 ± 1.4	9.02 ± 0.15	299/181	5.39 ± 0.18	21.59 ± 0.68	9.25 ± 0.18	287/181
150621282	0.77 ± 0.15	23.3 ± 3.7	6.58 ± 0.67	236/181	6.92 ± 0.64	13.4 ± 1.9	6.34 ± 0.30	220/181
150621289	0.726 ± 0.054	19.2 ± 1.3	10.46 ± 0.24	269/181	4.94 ± 0.16	18.75 ± 0.61	10.43 ± 0.22	254/181
150621298	0.276 ± 0.047	21.2 ± 1.2	52.50 ± 0.89	146/ 89	6.21 ± 0.18	22.46 ± 0.78	53.8 ± 1.1	126/ 89
150621327	0.576 ± 0.035	20.63 ± 0.99	24.33 ± 0.33	361/181	5.32 ± 0.13	20.68 ± 0.43	24.76 ± 0.31	335/181

Table 1:: continued from previous page

bn	Index[a]	E_{cut}[a] keV	Luminosity[a,b] 10^{37}erg cm^{-2}	Chi/dof	Electron Temp.[c] keV	Seed Photon Temp.[c] keV	Luminosity[b,c] 10^{37}erg cm^{-2}	χ^2/dof
150621335	0.295 ± 0.091	14.3 ± 5.2	12.18 ± 0.79	205/181	4.52 ± 0.48	25.9 ± 1.7	12.76 ± 0.59	201/181
150621344	1.562 ± 0.030	37.87 ± 0.89	25.79 ± 0.24	1031/273	3.116 ± 0.079	22.22 ± 0.29	26.99 ± 0.32	811/273
150621366	0.217 ± 0.060	21.9 ± 1.8	6.91 ± 0.17	463/273	6.70 ± 0.25	21.93 ± 0.91	7.04 ± 0.13	440/273
150621657	0.455 ± 0.017	16.32 ± 0.65	23.48 ± 0.15	356/181	4.762 ± 0.077	23.02 ± 0.29	24.18 ± 0.20	299/181
150621744	0.009 ± 0.011	$3.587 \pm 9772.$	$18.850 \pm 3504.$	1091/365	5.353 ± 0.066	28.66 ± 0.26	20.16 ± 0.10	928/365
150622002	1.339 ± 0.080	40.3 ± 2.2	10.14 ± 0.33	324/181	3.10 ± 0.21	27.82 ± 0.84	11.57 ± 0.31	219/181
150622018	0.384 ± 0.016	11.0 ± 2.3	12.10 ± 0.14	1465/457	4.030 ± 0.089	25.89 ± 0.35	12.70 ± 0.11	1388/457
150622027	0.623 ± 0.067	16.1 ± 2.0	9.99 ± 0.30	347/273	4.24 ± 0.22	22.06 ± 0.91	10.24 ± 0.29	339/273
150622071	-0.70 ± 0.19	24.7 ± 8.5	5.12 ± 0.90	897/273	10.5 ± 1.2	28.4 ± 3.4	5.40 ± 0.33	897/273
150622079	0.51 ± 0.14	34.9 ± 3.5	5.52 ± 0.72	185/181	6.37 ± 0.47	25.8 ± 1.8	5.82 ± 0.25	179/181
150622086	0.83 ± 0.13	64.2 ± 4.8	5.74 ± 0.79	223/181	8.70 ± 0.84	26.8 ± 2.9	6.42 ± 0.44	220/181
150622187	0.882 ± 0.096	35.1 ± 2.3	8.63 ± 0.43	269/181	5.19 ± 0.30	23.6 ± 1.0	8.90 ± 0.26	261/181
150622212	0.937 ± 0.093	20.5 ± 2.1	5.84 ± 0.21	270/181	4.86 ± 0.23	16.56 ± 0.89	5.74 ± 0.17	241/181
150622225	1.099 ± 0.039	72.0 ± 1.9	12.25 ± 0.19	293/ 89	7.15 ± 0.26	28.8 ± 1.0	14.09 ± 0.29	100/ 89
150622256	0.826 ± 0.044	23.3 ± 1.0	12.63 ± 0.19	439/181	5.98 ± 0.14	15.93 ± 0.45	12.33 ± 0.15	334/181
150622451	1.442 ± 0.035	81.8 ± 2.1	11.92 ± 0.24	261/181	5.56 ± 0.25	30.17 ± 0.98	13.10 ± 0.25	211/181
150622470	0.428 ± 0.043	21.9 ± 1.2	15.98 ± 0.26	402/181	6.27 ± 0.16	19.80 ± 0.54	16.11 ± 0.22	352/181
150622672	0.374 ± 0.026	19.05 ± 0.94	13.81 ± 0.11	641/365	5.41 ± 0.11	23.10 ± 0.40	14.35 ± 0.15	583/365
150622684	0.306 ± 0.035	15.0 ± 1.6	10.96 ± 0.14	601/457	5.13 ± 0.18	23.79 ± 0.67	11.27 ± 0.21	603/457
150623198	0.765 ± 0.080	32.8 ± 2.0	13.12 ± 0.42	572/365	4.43 ± 0.22	27.63 ± 0.88	14.17 ± 0.32	495/365
150623272	0.537 ± 0.066	20.5 ± 1.7	6.15 ± 0.13	290/181	6.04 ± 0.25	18.26 ± 0.87	6.08 ± 0.11	279/181
150623311	0.307 ± 0.060	16.2 ± 2.4	13.69 ± 0.41	242/181	5.14 ± 0.29	23.9 ± 1.0	14.05 ± 0.35	237/181
150623339	1.347 ± 0.054	134.6 ± 5.9	5.30 ± 0.26	472/457	5.32 ± 0.61	50.0 ± 3.3	6.47 ± 0.30	462/457
150623348	1.42 ± 0.12	$177.0 \pm 26.$	3.58 ± 0.66	295/273	4.8 ± 1.5	$54.9 \pm 10.$	4.33 ± 0.52	289/273
150623443	0.763 ± 0.013	16.80 ± 0.39	39.65 ± 0.21	801/181	4.132 ± 0.043	20.59 ± 0.16	40.46 ± 0.21	607/181
150623473	1.387 ± 0.027	120.0 ± 2.5	18.51 ± 0.37	1143/457	6.41 ± 0.25	38.9 ± 1.1	21.84 ± 0.47	808/457
150623482	0.110 ± 0.022	19.39 ± 0.73	15.99 ± 0.12	547/273	6.17 ± 0.10	25.21 ± 0.41	16.79 ± 0.18	468/273
150623515	0.776 ± 0.077	17.0 ± 2.3	14.84 ± 0.58	238/181	4.17 ± 0.25	20.16 ± 0.94	15.03 ± 0.51	235/181
150623526	1.06 ± 0.25	20.5 ± 6.6	13.8 ± 2.7	239/181	4.62 ± 0.63	15.7 ± 1.9	13.7 ± 1.1	234/181
150623715	0.990 ± 0.055	20.5 ± 1.2	14.05 ± 0.32	787/273	4.73 ± 0.13	16.45 ± 0.50	13.80 ± 0.20	744/273
150623722	0.614 ± 0.016	15.13 ± 0.63	30.61 ± 0.26	941/273	4.294 ± 0.067	21.52 ± 0.23	31.03 ± 0.25	944/273
150623741	0.225 ± 0.041	19.2 ± 1.4	10.37 ± 0.14	387/181	5.80 ± 0.18	23.93 ± 0.64	10.71 ± 0.15	365/181
150623749	0.835 ± 0.043	23.2 ± 1.0	40.94 ± 0.55	282/ 89	5.93 ± 0.13	14.95 ± 0.48	39.33 ± 0.53	141/ 89
150624171	0.624 ± 0.042	19.9 ± 1.1	65.61 ± 0.84	219/181	5.20 ± 0.15	20.04 ± 0.55	66.2 ± 1.0	202/181
150624178	0.986 ± 0.035	21.94 ± 0.84	79.6 ± 1.0	545/273	5.076 ± 0.094	16.14 ± 0.32	78.25 ± 0.80	430/273
150624201	1.159 ± 0.062	20.5 ± 1.3	18.43 ± 0.41	1488/457	4.83 ± 0.13	13.24 ± 0.54	17.34 ± 0.30	1373/457
150624248	0.803 ± 0.043	33.8 ± 1.0	8.35 ± 0.11	1182/273	3.64 ± 0.12	32.91 ± 0.54	10.15 ± 0.13	457/273
150624303	1.342 ± 0.053	173.0 ± 9.8	5.47 ± 0.24	211/181	6.08 ± 0.68	55.8 ± 4.5	6.63 ± 0.43	184/181
150624386	1.411 ± 0.028	87.8 ± 1.9	5.105 ± 0.084	516/273	6.14 ± 0.22	30.47 ± 0.92	5.54 ± 0.10	531/273
150624445	1.297 ± 0.058	108.6 ± 4.3	4.15 ± 0.20	536/273	7.38 ± 0.52	34.2 ± 2.0	4.75 ± 0.19	477/273
150624568	1.109 ± 0.014	57.19 ± 0.55	34.20 ± 0.20	1865/181	6.601 ± 0.075	25.97 ± 0.28	38.47 ± 0.27	350/181

Table 1:: continued from previous page

bn	Index[a]	E_{cut}[a] keV	Luminosity[a,b] 10^{37}erg cm^{-2}	Chi/dof	Electron Temp.[c] keV	Seed Photon Temp.[c] keV	Luminosity[b,c] 10^{37}erg cm^{-2}	χ^2/dof
150624585	0.78 ± 0.10	23.3 ± 2.7	4.72 ± 0.19	286/181	6.49 ± 0.39	14.0 ± 1.2	4.54 ± 0.12	249/181
150624599	0.108 ± 0.097	20.9 ± 3.3	6.98 ± 0.38	913/457	5.95 ± 0.42	27.2 ± 1.5	7.57 ± 0.30	891/457
150624724	0.302 ± 0.049	22.1 ± 1.4	14.66 ± 0.29	211/181	6.43 ± 0.19	21.82 ± 0.66	14.99 ± 0.23	200/181
150625186	0.978 ± 0.097	63.2 ± 3.2	5.94 ± 0.44	547/457	8.28 ± 0.55	27.1 ± 1.7	6.63 ± 0.21	542/457
150625263	0.151 ± 0.015	18.38 ± 0.57	14.695 ± 0.092	2413/457	5.590 ± 0.076	26.60 ± 0.30	15.72 ± 0.11	2084/457
150625296	0.330 ± 0.034	17.8 ± 1.1	13.76 ± 0.19	298/181	5.34 ± 0.14	23.81 ± 0.59	14.34 ± 0.19	270/181
150625363	0.98 ± 0.12	74.7 ± 5.0	7.59 ± 0.76	242/181	7.16 ± 0.79	36.7 ± 3.5	9.66 ± 0.74	211/181
150625370	1.221 ± 0.027	115.0 ± 2.1	10.07 ± 0.18	700/273	7.42 ± 0.26	40.0 ± 1.1	12.05 ± 0.25	460/273
150625392	0.251 ± 0.026	20.52 ± 0.80	18.11 ± 0.18	2115/457	6.55 ± 0.11	21.24 ± 0.41	18.30 ± 0.19	2094/457
150625400	0.359 ± 0.062	17.8 ± 2.1	41.9 ± 1.3	1239/457	5.24 ± 0.27	23.5 ± 1.0	43.4 ± 1.1	1229/457
150625498	1.237 ± 0.080	64.3 ± 3.7	10.16 ± 0.51	263/181	6.47 ± 0.48	25.9 ± 1.8	11.24 ± 0.42	234/181
150625530	0.524 ± 0.067	23.2 ± 1.7	8.79 ± 0.19	476/365	6.25 ± 0.22	19.27 ± 0.77	8.81 ± 0.17	472/365
150625899	1.181 ± 0.046	89.8 ± 2.8	11.50 ± 0.30	329/273	7.32 ± 0.39	33.3 ± 1.6	12.98 ± 0.41	360/273
150625921	0.657 ± 0.063	21.9 ± 1.6	8.51 ± 0.20	390/273	5.68 ± 0.20	18.15 ± 0.72	8.46 ± 0.16	344/273
150625928	0.252 ± 0.061	20.5 ± 1.9	15.52 ± 0.35	642/457	5.88 ± 0.26	24.31 ± 0.97	16.28 ± 0.43	623/457
150625976	0.626 ± 0.055	33.8 ± 1.3	9.65 ± 0.21	616/365	5.57 ± 0.17	26.21 ± 0.68	10.19 ± 0.16	564/365
150625984	-0.041 ± 0.079	14.5 ± 4.9	4.95 ± 0.27	390/365	5.46 ± 0.47	29.8 ± 1.9	5.39 ± 0.28	380/365
150625993	0.070 ± 0.019	19.61 ± 0.64	29.19 ± 0.21	1259/181	6.391 ± 0.090	25.30 ± 0.35	30.70 ± 0.21	1172/181
150626063	0.43 ± 0.13	20.4 ± 3.6	14.5 ± 1.0	214/181	5.75 ± 0.48	21.0 ± 1.9	14.82 ± 0.73	207/181
150626092	1.310 ± 0.022	83.4 ± 1.4	12.69 ± 0.17	757/181	6.38 ± 0.16	31.52 ± 0.72	14.62 ± 0.19	358/181
150626109	1.325 ± 0.077	114.6 ± 7.5	6.28 ± 0.43	189/181	6.43 ± 0.75	38.3 ± 3.8	6.97 ± 0.45	198/181
150626124	1.026 ± 0.030	53.8 ± 1.0	22.70 ± 0.25	995/181	6.26 ± 0.14	27.64 ± 0.59	26.09 ± 0.31	617/181
150626156	0.989 ± 0.055	77.9 ± 2.3	22.65 ± 0.72	406/273	8.64 ± 0.40	31.6 ± 1.4	26.37 ± 0.78	346/273
150626163	-0.004 ± 0.082	19.1 ± 3.2	9.77 ± 0.42	413/273	6.54 ± 0.42	26.4 ± 1.6	10.43 ± 0.45	402/273
150626170	1.127 ± 0.040	78.6 ± 1.9	10.27 ± 0.24	365/181	7.26 ± 0.28	30.9 ± 1.1	11.89 ± 0.25	253/181
150626177	0.915 ± 0.098	62.8 ± 3.3	11.19 ± 0.87	280/181	7.79 ± 0.53	28.9 ± 1.8	13.11 ± 0.47	230/181
150626184	1.273 ± 0.057	76.2 ± 3.0	8.74 ± 0.32	247/181	6.00 ± 0.38	30.7 ± 1.6	9.84 ± 0.38	226/181
150626192	1.203 ± 0.077	108.2 ± 6.0	14.42 ± 0.98	438/273	7.19 ± 0.69	34.9 ± 3.1	16.30 ± 0.81	402/273
150626222	1.375 ± 0.036	94.4 ± 2.7	30.08 ± 0.80	249/181	5.70 ± 0.29	34.4 ± 1.3	34.2 ± 1.1	186/181
150626230	1.07 ± 0.15	52.6 ± 5.3	14.2 ± 1.6	320/273	6.62 ± 0.70	24.9 ± 2.5	15.89 ± 0.99	303/273
150626238	0.150 ± 0.043	13.3 ± 3.0	8.18 ± 0.19	299/273	4.90 ± 0.24	28.0 ± 1.0	8.82 ± 0.20	271/273
150626253	-0.068 ± 0.053	17.7 ± 2.3	6.96 ± 0.16	364/181	6.41 ± 0.28	27.4 ± 1.1	7.45 ± 0.18	345/181
150626260	0.000 ± 0.029	22.00 ± 0.94	13.55 ± 0.12	470/181	6.98 ± 0.12	25.46 ± 0.48	14.28 ± 0.17	407/181
150626487	0.416 ± 0.018	15.33 ± 0.95	43.54 ± 0.30	574/181	4.655 ± 0.098	24.08 ± 0.33	45.39 ± 0.36	483/181
150626494	0.296 ± 0.019	18.09 ± 0.66	37.05 ± 0.26	1110/273	5.168 ± 0.087	25.69 ± 0.34	39.69 ± 0.36	887/273
150626518	1.04 ± 0.11	22.2 ± 2.7	14.48 ± 0.63	503/181	6.7 ± 2.4	$7.8 \pm 10.$	13.2 ± 6.3	428/181
150626553	0.892 ± 0.035	17.89 ± 0.71	77.64 ± 0.73	920/273	4.281 ± 0.072	17.95 ± 0.38	76.1 ± 1.2	834/273
150626564	0.480 ± 0.044	21.9 ± 1.1	27.85 ± 0.53	735/273	5.94 ± 0.16	20.32 ± 0.60	28.16 ± 0.44	693/273
150626577	1.097 ± 0.099	20.6 ± 2.1	66.4 ± 3.5	311/181	4.66 ± 0.22	15.39 ± 0.83	64.8 ± 1.8	288/181
150626593	0.751 ± 0.088	18.5 ± 2.3	57.3 ± 2.3	203/181	4.50 ± 0.27	20.0 ± 1.0	58.1 ± 1.9	199/181
150626620	1.02 ± 0.14	17.8 ± 3.2	41.6 ± 4.1	544/181	3.95 ± 0.32	17.8 ± 1.4	41.6 ± 1.9	542/181

Table 1:: continued from previous page

bn	Index[a]	E_{cut}[a] keV	Luminosity[a,b] 10^{37}erg cm^{-2}	Chi/dof	Electron Temp.[c] keV	Seed Photon Temp.[c] keV	Luminosity[b,c] 10^{37}erg cm^{-2}	χ^2/dof
150626627	0.870 ± 0.023	14.13 ± 0.81	32.50 ± 0.33	325/181	3.443 ± 0.075	20.93 ± 0.30	33.65 ± 0.34	248/181
150626636	1.78 ± 0.14	26.0 ± 4.2	40.2 ± 4.0	344/273	3.03 ± 0.26	16.2 ± 1.0	41.1 ± 1.9	350/273
150626643	1.017 ± 0.057	16.7 ± 1.4	37.63 ± 0.71	527/365	3.71 ± 0.14	18.53 ± 0.55	38.01 ± 0.69	522/365
150626652	0.641 ± 0.048	17.9 ± 1.3	15.54 ± 0.24	321/181	4.72 ± 0.15	20.45 ± 0.61	15.72 ± 0.26	308/181
150626685	0.984 ± 0.057	20.8 ± 1.2	73.8 ± 1.5	255/181	4.69 ± 0.13	16.87 ± 0.56	72.6 ± 1.3	242/181
150626724	0.816 ± 0.015	19.39 ± 0.36	69.79 ± 0.32	1649/181	4.610 ± 0.039	18.92 ± 0.17	70.01 ± 0.38	1418/181
150626751	0.889 ± 0.022	16.55 ± 0.54	66.51 ± 0.53	654/181	3.895 ± 0.055	19.47 ± 0.26	67.32 ± 0.57	622/181
150626766	0.304 ± 0.040	19.9 ± 1.1	46.47 ± 0.79	769/273	5.59 ± 0.16	24.43 ± 0.68	49.06 ± 0.89	745/273
150626773	1.261 ± 0.033	34.75 ± 0.92	23.19 ± 0.29	926/457	3.814 ± 0.091	22.92 ± 0.36	24.06 ± 0.24	755/457
150626781	1.078 ± 0.038	30.3 ± 1.1	18.96 ± 0.33	261/ 89	4.06 ± 0.10	22.92 ± 0.47	19.96 ± 0.26	110/ 89
150626788	0.592 ± 0.039	21.93 ± 0.98	52.87 ± 0.65	378/181	5.70 ± 0.12	19.31 ± 0.47	53.04 ± 0.66	331/181
150626822	0.843 ± 0.094	33.3 ± 2.4	14.96 ± 0.80	227/181	5.47 ± 0.31	22.3 ± 1.2	15.25 ± 0.52	227/181
150626829	0.430 ± 0.062	23.3 ± 1.6	15.48 ± 0.46	218/181	7.04 ± 0.24	17.73 ± 0.81	15.26 ± 0.29	200/181
150626844	0.170 ± 0.034	15.5 ± 1.5	13.32 ± 0.23	250/181	5.38 ± 0.18	25.44 ± 0.72	13.84 ± 0.25	251/181
150626851	0.008 ± 0.036	14.4 ± 2.3	13.48 ± 0.29	671/365	5.99 ± 0.22	26.61 ± 0.90	14.20 ± 0.32	665/365
150626888	1.262 ± 0.062	86.9 ± 3.9	6.39 ± 0.25	229/181	6.47 ± 0.49	33.0 ± 2.1	7.22 ± 0.29	232/181
150626896	1.393 ± 0.055	88.1 ± 3.7	6.22 ± 0.25	328/273	5.04 ± 0.43	36.4 ± 2.0	7.27 ± 0.29	316/273
150626903	1.477 ± 0.053	$172.7 \pm 11.$	5.41 ± 0.27	169/181	4.44 ± 0.63	50.4 ± 3.9	6.13 ± 0.43	161/181
150626910	1.402 ± 0.036	104.7 ± 3.0	7.94 ± 0.20	989/365	5.79 ± 0.32	37.6 ± 1.5	9.16 ± 0.27	949/365
150626918	1.205 ± 0.022	114.7 ± 2.1	17.32 ± 0.27	646/181	6.97 ± 0.21	42.4 ± 1.2	21.25 ± 0.53	403/181
150626957	0.086 ± 0.068	$0.00 \pm 277.$	$5.5 \pm 48.$	658/457	2.11 ± 0.71	38.1 ± 1.8	6.99 ± 0.44	571/457
150626979	1.340 ± 0.046	108.4 ± 3.8	5.73 ± 0.19	323/273	5.95 ± 0.42	38.8 ± 2.0	6.78 ± 0.23	260/273
150626989	1.329 ± 0.073	104.8 ± 6.9	2.47 ± 0.14	336/273	4.72 ± 0.60	44.8 ± 4.1	3.13 ± 0.22	307/273
150627023	1.296 ± 0.031	75.7 ± 1.6	11.76 ± 0.18	567/273	5.96 ± 0.21	31.16 ± 0.87	13.39 ± 0.24	447/273
150627030	-0.607 ± 0.051	$6.885 \pm 2311.$	$7.52 \pm 252.$	391/273	5.37 ± 0.39	43.8 ± 2.0	9.52 ± 0.37	317/273
150627038	1.15 ± 0.10	112.7 ± 6.5	6.24 ± 0.53	596/457	7.81 ± 0.97	41.1 ± 4.2	7.28 ± 0.52	598/457
150627047	1.227 ± 0.054	128.3 ± 4.9	5.82 ± 0.26	310/181	5.94 ± 0.57	48.7 ± 3.3	7.24 ± 0.36	290/181
150627054	1.208 ± 0.062	163.1 ± 8.9	8.41 ± 0.49	245/181	7.07 ± 0.78	53.5 ± 4.8	10.15 ± 0.74	236/181
150627082	1.170 ± 0.082	90.3 ± 4.7	6.90 ± 0.48	252/181	7.71 ± 0.66	32.7 ± 2.6	7.92 ± 0.42	232/181
150627091	1.372 ± 0.050	148.1 ± 6.7	6.05 ± 0.31	475/273	7.80 ± 0.56	35.6 ± 2.2	6.46 ± 0.28	412/273
150627162	1.453 ± 0.023	137.0 ± 2.9	8.05 ± 0.13	382/273	4.72 ± 0.25	45.4 ± 1.3	9.30 ± 0.16	337/273
150627978	1.294 ± 0.059	125.3 ± 6.0	4.75 ± 0.21	223/181	6.67 ± 0.62	42.9 ± 3.3	5.60 ± 0.36	220/181

[a] The index and high energy cut-off from the POWERLAW*HIGHECUT model

[b] Luminosity is calculated from 10-1000 keV

[c] The electron temperature and seed photon temperature from the CompTT model